Joule

CellPress
OPEN ACCESS

Article

Stepwise photoassisted decomposition of carbohydrates to H_2

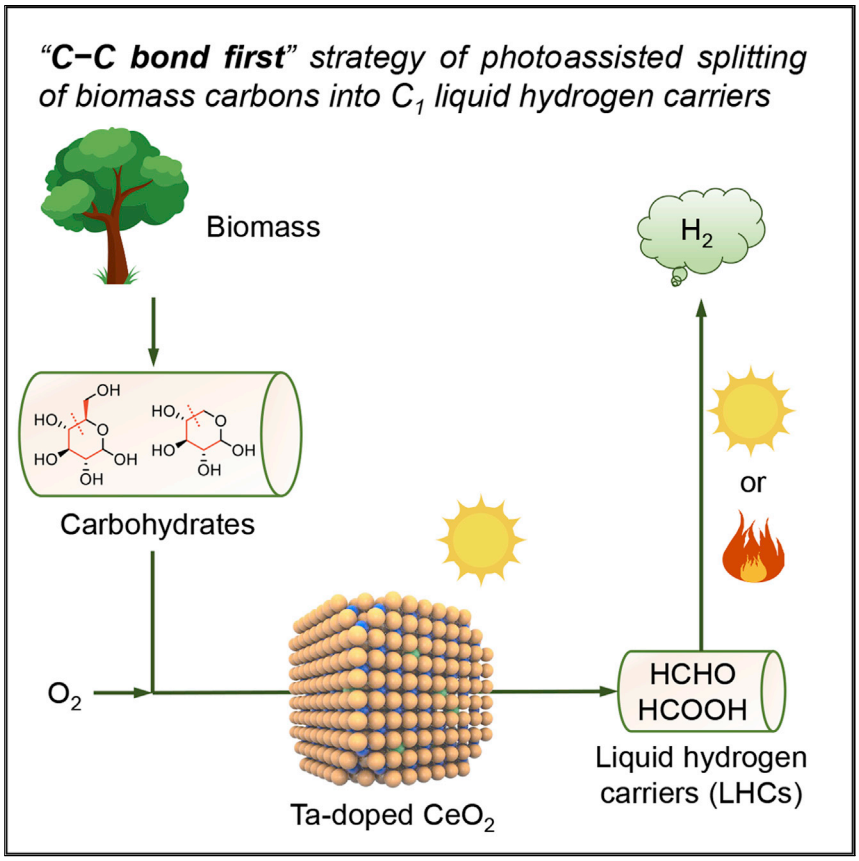

Biomass photoreforming is an advanced way of providing sustainable H_2, whereas a maximized H_2 yield relies on high extent of C–C bond breaking. Here, relying on a "C–C bond first" strategy that C–C bonds of carbohydrates are broken first over Ta-CeO_2, carbohydrates are converted to C_1 liquid hydrogen carriers (LHCs, consisting of HCOOH and HCHO), which release H_2 in high yield when degrading. This work realizes bio-H_2 production and storage and provides a new perspective for bio-H_2 production by photocatalysis.

Puning Ren, Zhuyan Gao, Tiziano Montini, ..., Emiliano Fonda, Paolo Fornasiero, Feng Wang

ncluo@dicp.ac.cn (N.L.)
pfornasiero@units.it (P.F.)
wangfeng@dicp.ac.cn (F.W.)

Highlights

Stepwise carbohydrate decomposition realizes H_2 production and storage

Photocatalysis over Ta-CeO_2 splits carbohydrates into C_1 LHCs

Heating promotes selective C–C bond breaking powered by visible light

Concentrated solar light splits glucose to C_1 LHCs in a flow apparatus

Ren et al., Joule 7, 333–349
February 15, 2023
Published by Elsevier Inc.
https://doi.org/10.1016/j.joule.2023.01.002

Joule

CellPress
OPEN ACCESS

Article

Stepwise photoassisted decomposition of carbohydrates to H_2

Puning Ren,[1,2,8] Zhuyan Gao,[1,2,8] Tiziano Montini,[3,8] Zhitong Zhao,[4] Na Ta,[5] Yike Huang,[2,6] Nengchao Luo,[1,*] Emiliano Fonda,[7] Paolo Fornasiero,[3,*] and Feng Wang[1,9,*]

SUMMARY

Biomass reforming by harvesting solar energy can provide green hydrogen. Current biomass photoreforming provides H_2 erratically and in limited yield although efficiently, owing to intermittent features of solar light and incomplete degradation of biomass C–C bonds. Here, we detour the flaws by prioritizing conversion of carbohydrates to liquid hydrogen carriers (LHCs, consisting of HCOOH and HCHO), appropriate for transportation. Subsequently, the LHCs are fully decomposed, releasing only H_2 and CO_2. This stepwise process enables complete scission of carbohydrate C–C bonds, affording 44 g of H_2 per kg of glucose thereof. Intermittent solar light provides the photoenergy and heat to split glucose carbons to produce LHCs (2.5 mmol h^{-1}) in a flow apparatus. This work demonstrates hydrogen production and storage by emphasizing the complete scission of biomass C–C bonds.

INTRODUCTION

Hydrogen (H_2) has emerged as a sustainable and indispensable energy vector that can be produced from renewable energy resources.[1,2] Storage and transportation of H_2 remain challenging in the aspect of its worldwide applications.[3] In this context, formic acid (HCOOH) has been identified as a promising liquid hydrogen carrier (LHC), thermally stable up to 200°C,[4,5] easy to transport, and be back decomposed with H_2 release by thermo-, photo-, or electrocatalysis.[6–8] Therefore, a very promising and challenging way of exploiting the hydrogen economy is based on the use of HCOOH, which must be produced from renewable resources.[9,10] Broadly available next-generation biomasses containing both carbon and hydrogen are such kinds of renewable resources.[11,12] Both hydrogen production and storage can be achieved if biomass is converted to HCOOH. Cellulose, hemicelluloses, and their hydrolyzates can generate HCOOH by thermocatalysis,[9] processes that require stoichiometric oxidants with strong oxidation potential to break the C–C bonds. However, these carbohydrates suffer over-oxidation to CO_2 on catalysts.[13,14]

Producing strong oxidants to cleave C–C bonds represents the advantage of photocatalysis.[15,16] Carbohydrates are easily over-oxidized with less HCOOH generation because of the relatively long carbon chains; nevertheless, more H_2 is produced from carbohydrates concomitantly due to the charge balance of photocatalysts,[17] which is the current consensus of exploiting photogenerated oxidants for H_2 generation from biomass (Figure S1 path A).[18] The principle is to generate holes or •OH, which breaks the O–H bonds of biomass, mainly the carbohydrate components, generating oxygen-centered radicals that experience β-scission to cleave the C–C

CONTEXT & SCALE

Hydrogen (H_2), as an indispensable clean energy vector, has been well demonstrated to be produced via biomass photoreforming powered by solar light. For future biomass refining, biomass photoreforming deserves a high decomposition extent of biomass to maximize H_2 production, as the greenhouse gas emissions from biomass acquisition and pretreatment will minimize per mass of H_2. The main obstacle to high H_2 yield is the far insufficient C–C bond breaking to convert biomass carbons into CO_2 with maximization of H_2 production. Here, we emphasize C–C bond breaking instead of direct H_2 production. Such a "C–C bond first" strategy realizes conversion of carbohydrates into C_1 liquid hydrogen carriers (LHCs, consisting of HCOOH and HCHO) over Ta-CeO_2 photocatalyst and is demonstrated in a flow apparatus powered solely by solar energy. The LHCs can release H_2 on-site where needed by either photocatalysis or thermocatalysis. This work provides a new perspective for H_2 production by photocatalysis.

bonds.[19,20] However, the co-generated carbon-centered radicals and those derived from direct oxidation of the C–H bond by photogenerated oxidants tend to form C–C bonds when external or concurrently generated oxidants are absent (Figure S1 path B).[21,22] This mechanism of photochemical recondensation is adverse to C–C bond breaking, as biomass is converted to recalcitrant architecture like humin and wasted.[23] Neglecting the principle for C–C bond scission limits the amount of H_2 per mass of biomass.[18] Besides, the intermittent feature of solar light provides H_2 erratically. Tackling these challenges requires prioritized biomass conversion to HCOOH or equivalent C_1 LHCs, appropriate for on-site hydrogen production independent of solar light irradiation.[24,25] However, fully breaking the C–C bonds to produce these active C_1 LHCs is challenging, as the C_1 LHCs are readily decomposed into side products either on photocatalysts or with the catalysis of acids generated concurrently.[26]

In an approach orthogonal to direct H_2 production from biomass, here we devise the strategy of "C–C bond first" that carbohydrates from hydrolysis of lignocellulose are first converted to LHCs with nearly 100% yield of C_1 products (Figure 1). Subsequent degradation of the LHCs provides H_2 and CO_2 exclusively. The photocatalytic oxidation of carbohydrates in the first step targets splitting carbohydrate carbons into C_1 LHCs, distinct from those reported for oxidative functionalization of carbohydrates. This oxidation step was conducted over strongly distorted Ta-doped CeO_2 (Ta-CeO_2), and the kinetics of C–C bond scission, C–C bond coupling, and conversion of recalcitrant carbonyl intermediates were controlled to realize a high LHCs selectivity. The obtained aqueous solution of LHCs releases gaseous H_2 where needed by either photocatalysis or thermocatalysis. Solar-light-driven catalytic oxidation of glucose in a flow apparatus demonstrates the allure of the biomass conversion to LHCs.

RESULTS AND DISCUSSION

Structure of Ta-CeO_2 photocatalyst

The Ta content of Ta-CeO_2 was determined to be 0.78 mol % by inductively coupled plasma atomic emission spectroscopy (ICP-AES). X-ray diffraction (XRD) patterns (Figure S2A) of CeO_2, the contrast catalyst, and Ta-CeO_2 show fluorite structure. The diffraction peaks of Ta-CeO_2 negligibly shift (Figure S2B), in agreement with the low amount of Ta dopant. Representative high-angle annular dark-field scanning transmission electron microscopy (HAADF-STEM) image of the Ta-CeO_2 shows the morphology of a rectangular structure (Figure 2A) with an average size of about 7.7 nm (Figure S3). The lattice fringes with spacings of 0.27 and 0.29 nm (Figure 2A) are attributed to the (200) and (020) interplanar distances of fluorite CeO_2, respectively. The HAADF-STEM image and the elemental mappings by energy-dispersive X-ray spectra (EDS) show the uniform dispersion of Ta and Ce elements (Figure 2B), implying that Ta is homogeneously incorporated into the matrix of CeO_2 (Figure 2C).

The inclusion of Ta in the CeO_2 matrix is confirmed by X-ray absorption fine structure (XAFS) analysis of the Ta-CeO_2 sample at the Ta L_3 edge. The X-ray absorption near edge structure (XANES) spectrum of the Ta-CeO_2 (Figure 2D) shows that Ta is in the +5 oxidation state as in Ta_2O_5. The fitting of the k^1-weighted extended X-ray absorption fine structure (EXAFS) signal (Figure 2E) reveals that the average local structure around Ta atoms can be reconstructed, including ~8 oxygen atoms at two different Ta–O distances and ~2 Ce atoms in the second shell (results are summarized in Table S2). The possibility of observing a Ta–Ce distance in the second shell is a clear indication of the substitution of Ta^{5+} for Ce^{4+} in the CeO_2 matrix. Despite this, the local environment around Ta ions is strongly distorted with respect to the

[1]State Key Laboratory of Catalysis, Dalian National Laboratory for Clean Energy, Dalian Institute of Chemical Physics, Chinese Academy of Sciences, Dalian 116023, China

[2]University of Chinese Academy of Sciences, Beijing 100049, China

[3]Department of Chemical and Pharmaceutical Sciences, Center for Energy, Environment and Transport Giacomo Ciamician, INSTM Trieste Research Unit and ICCOM-CNR Trieste Research Unit, University of Trieste, Via Licio Giorgieri 1, Trieste 34127, Italy

[4]College of Chemical Engineering and Technology, Taiyuan University of Technology, Taiyuan, Shanxi 030024, China

[5]State Key Laboratory of Catalysis, Dalian Institute of Chemical Physics, Chinese Academy of Sciences, Dalian 116023, China

[6]Laboratory of Catalysts and New Materials, Dalian Institute of Chemical Physics, Chinese Academy of Sciences, Dalian 116023, China

[7]Synchrotron SOLEIL, L'Orme des Merisiers, Saint Aubin BP48, 91192 Gif sur Yvette Cedex, France

[8]These authors contributed equally

[9]Lead contact

*Correspondence: ncluo@dicp.ac.cn (N.L.), pfornasiero@units.it (P.F.), wangfeng@dicp.ac.cn (F.W.)

https://doi.org/10.1016/j.joule.2023.01.002

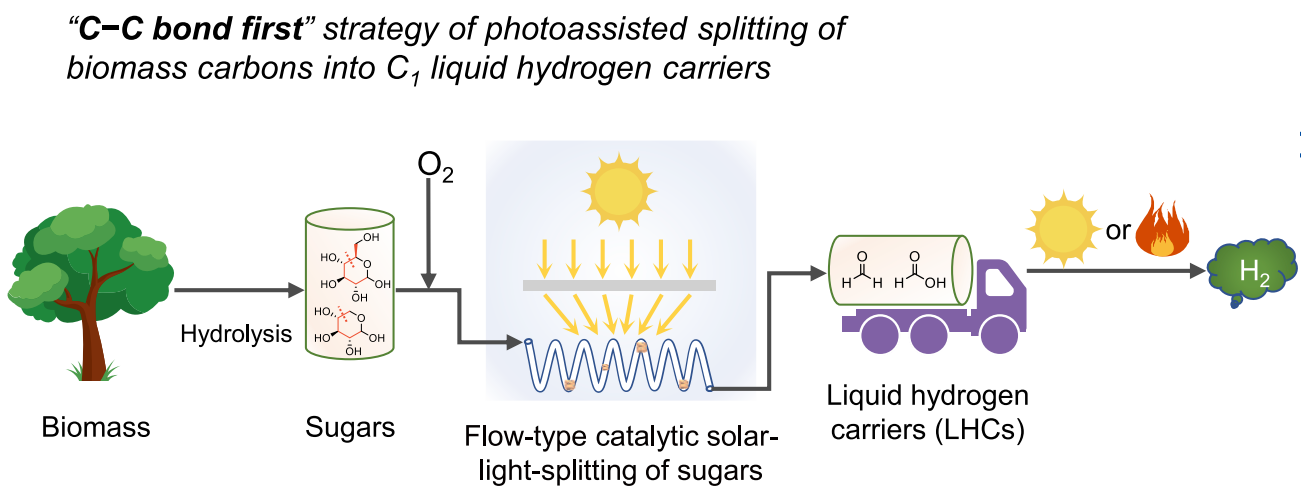

Figure 1. Illustration of a stepwise method for H_2 production from biomass and storage in the form of C_1 LHCs

Orthogonal to direct H_2 production from biomass, the diagram highlights a C–C bond first strategy that C–C bonds of biomass are broken firstly and the biomass carbons are split into LHCs. The term C_1 LHCs denotes C_1 chemicals in the form of liquid or well dissolved in water at room temperature and atmospheric pressure. This strategy maximizes biomass utilization for a high H_2 yield if decomposing the LHCs. Cellulose and hemicellulose components of lignocellulose are hydrolyzed to sugars, and their C–C bonds are fully broken by catalytic solar-light oxidation, affording C_1 products consisting of HCOOH and HCHO majorly. The two C_1 products are LHCs appropriate for transportation and can be fully converted for H_2 release by either photocatalysis or thermocatalysis.

cubic symmetry of the site hosting the cations in the fluorite structure of CeO_2, in agreement with HAADF-STEM results. Moreover, the Ta–O and Ta–Ce distances are significantly shorter than those expected for the fluorite structure of CeO_2 (Ce–O distance of 0.234 nm and Ce–Ce distance of 0.382 nm).[27] The strong lattice distortion of the local structure around Ta can be easily justified considering the ionic radii of Ta^{5+} and Ce^{4+} in the cubic coordination: 0.074 and 0.097 nm, respectively.[28] Considering the smaller ionic radius of Ta^{5+}, the local structure around Ta ions must be contracted with the oxygen anions moving toward the dopant, with consecutive relaxation of the successive shell of Ce ions. This distortion can be partially compensated by the formation of one Ce^{3+} expected in the proximity of each Ta^{5+} dopant as a result of charge compensation and that Ce^{3+} is larger than Ce^{4+} (ionic radii of 0.114 versus 0.097 nm),[28] in agreement with the results of Raman spectra (Figure S4). Compared with the as-prepared CeO_2, which has an indirect band gap of 2.60 eV (see Note S1), the band gap of Ta-CeO_2 is narrower (2.37 eV) owing to the lattice distortion and increased Ce^{3+} concentration (Figure S5).

Photocatalytic oxidation of glycerol to C_1 LHCs

In direct photoreforming of biomass, the biomass is partially oxidized, H_2 is thus produced in a limited yield, and biomass degrades to by-products that require tedious separations or disposal.[18] The underutilization of biomass originates from incomplete scission of biomass C–C bond and radical coupling in an environment lacking oxidative oxygen radicals, such as $O_2^{\bullet-}$ and •OH. Glycerol was used as a model molecule at the beginning of the research, although we realize that oxidative splitting of carbohydrate carbons is much more arduous than splitting glycerol carbons because of the longer carbon chains (Table S1). However, the simple and representative polyol structure is beneficial for intermediate detection and mechanism study. Photocatalytic oxidation of glycerol by O_2 (5 bar) was evaluated at near room temperature (36°C) over Ta-CeO_2 using a homemade photoreactor (Figures 3A and S6). The conversion of glycerol was 26%, and the yield of LHCs was 6% after

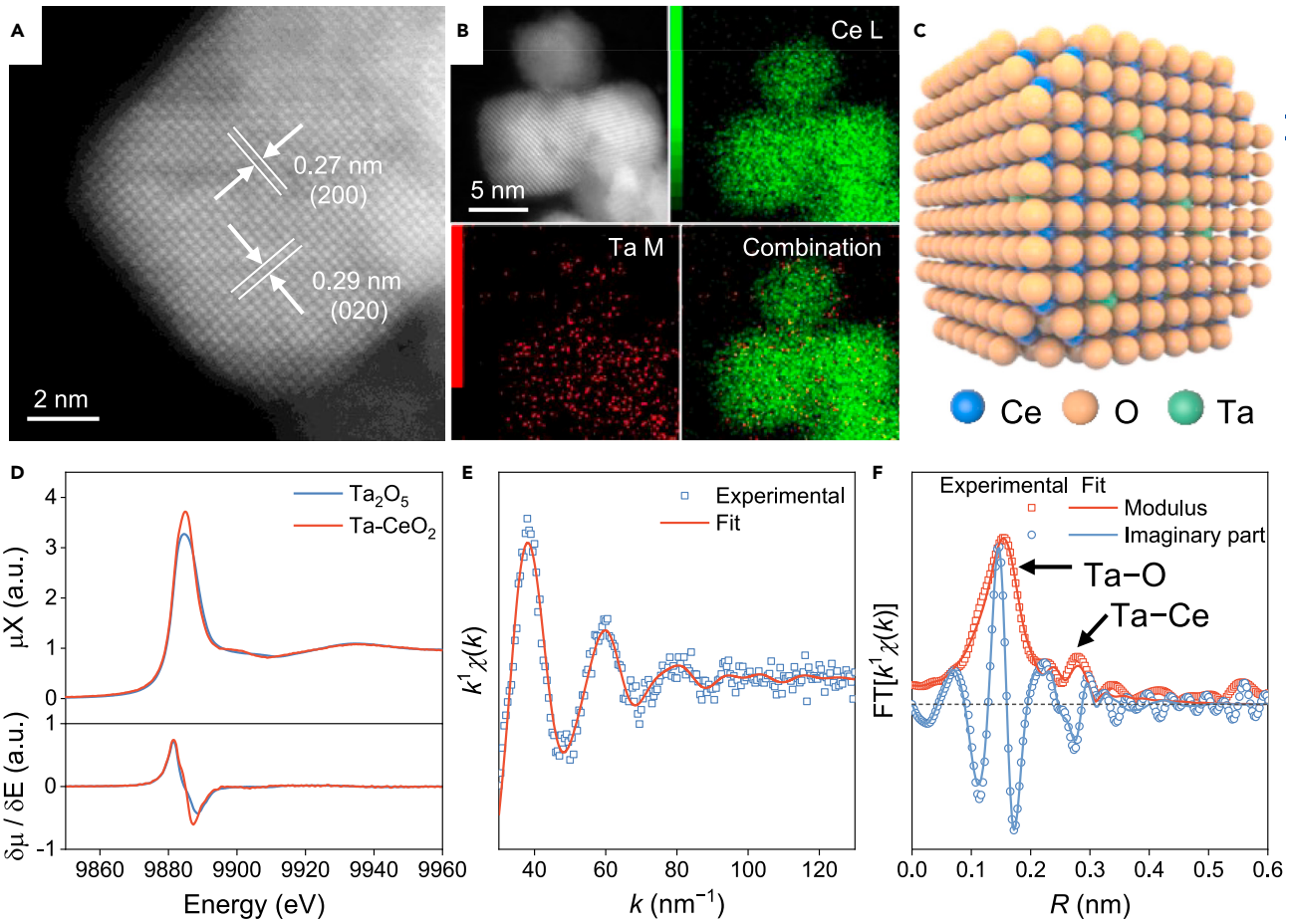

Figure 2. Characterization and structure of Ta-CeO_2 photocatalyst

(A) Representative HAADF-STEM image of Ta-CeO_2 nanoparticles.

(B) Representative HAADF-STEM image and EDS mappings recorded at Ce L and Ta M edges, and the combination.

(C) Crystal structure of Ta-CeO_2 built by referring to the HAADF-STEM results.

(D) XANES spectrum of Ta-CeO_2 at the Ta L_3 edge compared with that of the standard Ta_2O_5, as normalized spectra and first derivative.

(E and F) (E) The fitting of the k^1-weighted EXAFS signal at the Ta L_3 edge and (F), the correspondent Fourier transform.

photoirradiation for 10 h by blue light-emitting diodes (LEDs, 452 ± 10 nm, 200 mW cm^{-2}), indicating that C–C bonds were broken incompletely as widely reported.[29] The yield of LHCs was improved to 74% at 120°C, with glycerol conversion of 93% (43% apparent quantum efficiency). The photocatalytic glycerol oxidation can be conducted in air (25 bar), affording LHCs in 58% yield with glycerol conversion of 75% in a similar O_2 partial pressure (5 bar, Figure S8). The selectivity of LHCs (65%, Table S3, entry 1) reduces at a higher reaction temperature (150°C), owing to the prevalent over-oxidation of HCOOH to CO_2. This degradation of glycerol to LHCs also relies on photoirradiation, considering glycerol is scarcely converted in the dark even at 120°C (Figure S9A). Glycerol is converted to LHCs with high selectivity (80%) even irradiated with weak light intensity (18 mW cm^{-2}), indicating the synergy of photo and thermal is essential for the splitting of glycerol carbons. When irradiated with a light intensity larger than 130 mW cm^{-2}, the conversion of glycerol and selectivity of LHCs remained unchanged, illustrating that either the light absorption was saturated or the elementary steps involving photogenerated charges were no longer rate-limiting. Under the varied range of light intensities, the carbon balance which is defined as Equation 9 is within 95%–103% (Figure S9B).

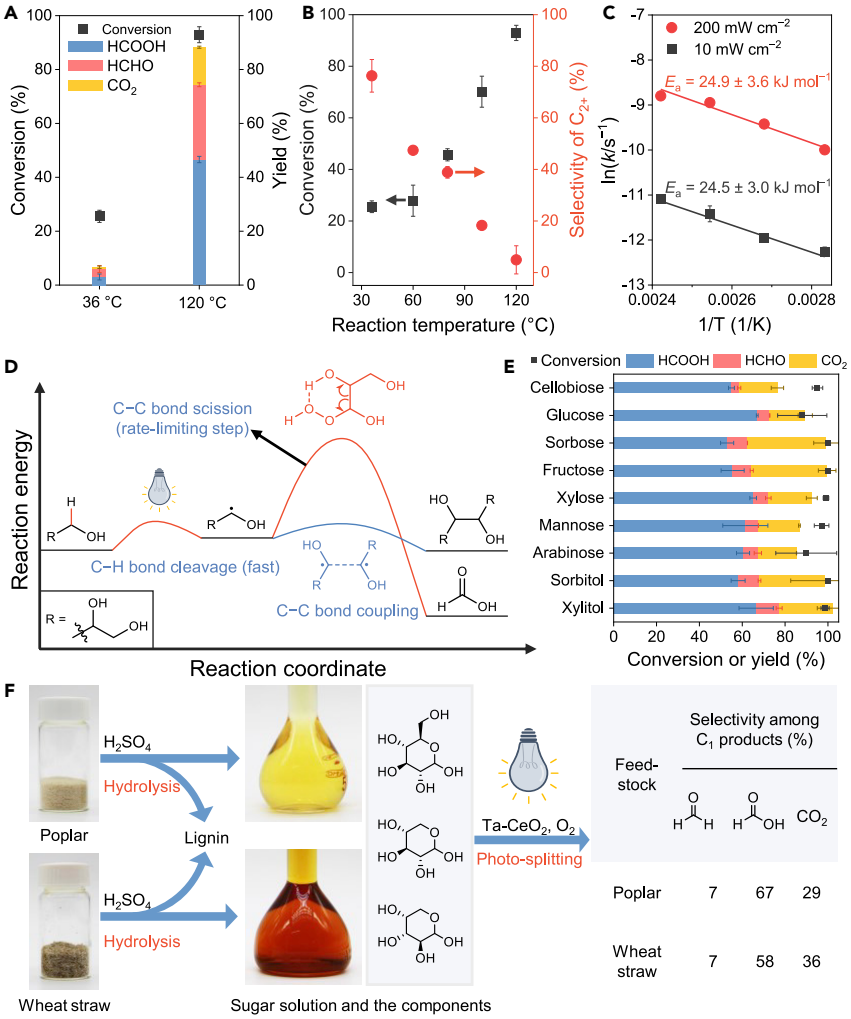

Figure 3. Reaction results and mechanism studies of photocatalytic oxidation of bio-polyols and sugars to C_1 LHCs

(A) Reaction results of photocatalytic glycerol oxidation at 36°C and 120°C, respectively.

(B) Conversion of glycerol and selectivity of C_{2+} products versus the reaction temperature. C_{2+} represents undetected products; their selectivity is calculated by subtracting C_1 products from all the products. Error bar represents the standard deviation.

(C) The Arrhenius plots of photocatalytic glycerol conversion under irradiation with light intensities of 10 and 200 mW cm^{-2}, respectively.

(D) Schematic diagram of the reaction coordinate for photocatalytic glycerol conversion at 36°C and 120°C, respectively.

(E) Reaction results of the photocatalytic oxidation of bio-polyols and sugars to LHCs at 120°C. The total carbons of each substrate were 9 mmol.

(F) Conversion of native biomass to LHCs. The powder of poplar and wheat straw was hydrolyzed by H_2SO_4, producing solutions of sugar mixture, which were then subjected to photocatalytic oxidation (20 and 25 h for poplar and wheat straw, respectively). The conversion of the sugar mixture from poplar and wheat straw was 55% and 52%, respectively.

Glycerol was converted rapidly in the first 2 h under the optimized reaction conditions and was entirely converted after reacting for 20 h, according to the time profiles; the final yield of LHCs reached 86% (Figure S10A). During photocatalytic glycerol oxidation, the carbon balance increased from 72% at 2 h to nearly 100% when glycerol was fully converted (Figure S10B). The Ta-CeO_2 photocatalyst shows minor deactivation during the first run and slightly higher deactivation (about 12% according to glycerol conversion) for the subsequent runs (Figure S11). The observed slight deactivation is not amazing and can be explained by the poisoning of Ta-CeO_2 by HCOOH or formaldehyde (HCHO) during photocatalysis.

LHCs consisting of HCHO and HCOOH could be produced over pristine CeO_2 in 58% yield (Table S3, entry 4) after 10 h of reaction at 120°C; the conversion of glycerol was 73%, lower than that (93%) using Ta-CeO_2. Of note, Ta-doped other metal oxides, such as TiO_2 and Nb_2O_5, are not selective to C_1 LHCs. The promotional role of Ta that is doped into CeO_2 could be attributed to the abundantly present Ce^{3+}, deriving from the substitution of Ta^{5+} for Ce^{4+} in the CeO_2 matrix (see Note S1). The higher concentration of Ce^{3+} in Ta-CeO_2 is expected to adsorb more reactant intermediates,[30,31] thereby breaking the C–C bond scission to produce LHCs in high selectivity. The high concentration of Ce^{3+} in Ta-CeO_2 also promotes electron transition from O 2p to Ce 4f orbits (Figure S12),[32] generating more photogenerated carriers for glycerol conversion. Doping Ta into CeO_2 can weaken the adsorption of HCHO and HCOOH on CeO_2 according to the results of temperature-programmed desorption (TPD) experiments (Figure S13; Note S6).[33]

We studied the reaction routes of the photocatalytic glycerol oxidation. The radical intermediates were captured by benzyl acrylate (BA) and 2,2,6,6-tetramethyl-1-piperidinyloxy (TEMPO). Quadrupole-time of flight mass spectrometer (Q-TOF MS) was used to analyze the products derived from the reaction of radical intermediates and trapping reagents. The adducts derived from the addition reaction of BA and glycerol were detected with the addition of 1 equivalent of BA (Figure S14A), implying that radicals derived from C–H bond scission were the intermediates. C_2 intermediates in the form of glycolaldehyde and glycolic acid were detected according to the m/z of 214 and 75 (Figure S14B), attributed to TEMPO-glycolaldehyde adduct and glycolic acid, respectively.[34] Photocatalytic scission of the C–C bonds in these C_2 intermediates also requires heat (Figure S15). Other intermediates were probed by control experiments. Photocatalytic conversion of hypothesized C_3 intermediates (Table S3, entries 6, 7, and 8), including glycerol acid, glyceraldehyde, and 1,3-dihydroxyacetone, produces LHCs with yields of 8%, 55%, and 47%, respectively, suggesting that glyceraldehyde and 1,3-dihydroxyacetone are partially involved in the photocatalytic glycerol oxidation. We also tried to reveal possible C_2 intermediates. Photocatalytic glycolaldehyde oxidation (Table S3, entry 9) was very fast, affording LHCs and CO_2 with 80% and 15% yields in 3 h, respectively. Photocatalytic oxidation of glycolic acid with prolonged reaction time (6 h) produced LHCs (25%) and CO_2 (27%) in low yields (Table S3, entry 10). The above results indicate that glycolaldehyde is the major intermediate and derives from the C–C bond scission of glycerol via the initial scission of the terminal C–H bond.

Tentative reaction routes were proposed for the photocatalytic glycerol oxidation (Figure S16), combing with the results that photogenerated holes, electrons, and $O_2^{\bullet-}$ are essential to the photocatalytic glycerol oxidation (Figure S17). Irradiation of Ta-CeO_2 generates holes and electrons. Photogenerated holes oxidize the C–H bond of glycerol, affording carbon-centered radicals mainly at the terminal carbon of glycerol (path I). The carbon-centered radicals react with $O_2^{\bullet-}$ derived from the reduction of O_2 by photogenerated electrons, bringing about C–C bond scission with the generation of glycolaldehyde and HCOOH. The glycolaldehyde then experiences C–C bond scission, producing HCOOH and HCHO in equal amounts. Parallel to this reaction path (path I), the C–C bond scission of carbon-centered radicals at the middle carbon produces HCOOH, HCHO, and CO_2 (path II).

Mechanism of the heat-assisted photocatalytic oxidation

We then studied the catalytic mechanism of heat in promoting photocatalytic oxidation of polyols by monitoring the selectivity of C_{2+} products, of which the selectivity could be calculated by subtracting C_1 products from all the products. A high

proportion of C–C bonds is retained at low reaction temperatures according to the moderate selectivity (76%) of C_{2+} products for photocatalytic glycerol oxidation at 36°C (Figure 3B). The selectivity of C_{2+} products decreases when improving the reaction temperature, with a selectivity of 5% at 120°C. The undetected carbons were analyzed by Q-TOF MS (Figure S18). In the high-resolution MS, the peaks with m/z of 89.0245, 191.0737, 211.0830, and 255.2341 are ascribed to $C_3H_6O_3$ and $C_6H_{10}O_4$, $C_8H_6O_4$, and $C_{10}H_{10}O_5$, respectively. The intensities of MS peaks were stronger at 36°C than those at 120°C, in agreement with the results depicted in Figure 3B. Particularly, $C_3H_6O_3$, ascribed to glyceraldehyde or 1,3-dihydroxyacetone, is produced from the dehydrogenation of glycerol, indicating that the elimination of H_2 molecule from glycerol is more overwhelming than breaking the C–C bonds of glycerol at low temperature (36°C). The formation of $C_6H_{10}O_4$, $C_8H_6O_4$, and $C_{10}H_{10}O_5$ during photocatalytic glycerol oxidation indicates a significant contribution of C–C bond coupling. Generally, the C–C bonds cannot be directly activated,[35,36] and their scission is generally less prone than the dehydrogenation of hydroxyl moieties and C–C bond coupling between two radicals.[37] Considering the above results, the low selectivity of C_{2+} products at high temperatures implies that heating may assist C–C bond scission. Therefore, both the products from dehydrogenation and C–C bond coupling are converted, preferentially generating HCOOH and HCHO.

To prove the hypothesis, we measured the apparent activation energy (E_a) and the kinetic isotope effect (KIE) in the photocatalytic glycerol oxidation. The E_a measured at low light intensity (10 mW cm^{-2}) represents that of dark conditions, considering glycerol is scarcely converted in the dark. The reaction rate constants, fitted from first-order kinetics (a linear relationship between the logarithm of glycerol concentration [$C_{glycerol}$] and the reaction time; Figure S19),[38] were obtained at various temperatures under irradiation with light intensities of 10 and 200 mW cm^{-2}, respectively (Figure 3C). The linear fit between the logarithm of rate constants and the reciprocal of the reaction temperature affords the E_a, which is determined to be 24.5 and 24.9 kJ mol^{-1} for the reactions with light intensities of 10 and 200 mW cm^{-2}, respectively. This result suggests that the rate-limiting step of photocatalytic glycerol oxidation is independent of light intensity. Because the trajectory of the photocatalytic glycerol oxidation involves C–H and C–C bond scission, the KIE experiments were designed to evaluate which step is of kinetic significance. The conversion rates of glycerol and deuterated glycerol were determined at 200 mW cm^{-2}. The KIE values for scission of the C–H bond at the middle and terminal carbons were measured to be 1.20 $\pm$ 0.02 and 1.19 $\pm$ 0.04, respectively (Table S4, entries 2 and 3). The secondary KIE values excluded the photocatalytic C–H bond scission as the rate-limiting step. Consequently, the C–C bond scission should be rate-limiting. Considering the E_a of the photocatalytic glycerol oxidation is barely influenced by light intensity, heating energy is expected to be crucial to overcoming the energy barrier in the C–C bond scission, as shown in Figure 3D.

Photocatalytic oxidation of sugars, bio-polyols, and native biomass to C_1 LHCs

Lignocellulose consists of cellulose, hemicelluloses, and lignin; the first two components account for 70% of lignocellulose. Through hydrolysis, enzymolysis, or hydrogenation, cellulose and hemicelluloses can be readily converted to monosaccharides and bio-polyols that feature vicinal polyhydroxy structures. These sugars and polyols were used as feedstocks to produce LHCs (Figures 3E and S20). Bio-polyols, including xylitol and sorbitol, are fully converted, with the C–C bond being fully broken after irradiation for 15 h. The yields of LHCs are 77% and 68%, respectively. Sugars, such as aldoses and ketoses, are converted into LHCs as well, and the LHCs yields are in the range of 62%–73%, slightly lower than those of bio-polyols. The

lower LHCs yields could be rationalized by the higher tendency of forming CO_2 when breaking the C–C bond adjacent to the formyl group. A longer reaction time is required for sugars than glycerol to split the carbons due to longer carbon chains; the selectivity of HCOOH is expected to be higher, considering HCHO can be slowly oxidized into HCOOH during reactions (Table S3, entry 11). Cellobiose, containing β-1,4-glycosidic linkage, represents the building units of cellulose and is converted to LHCs in 59% yield after irradiation for 20 h; besides LHCs, glucose is produced in 13% yield, which may be the intermediate of cellobiose. We tried to improve C_1 LHCs concentration by adding glucose into the reaction in batches and successfully increased the concentration of the produced LHCs from 1.2 to 6.9 wt % (Figure S22B). The above results demonstrate that the C–C bonds of common bio-polyols and sugars can be almost fully broken via oxidative photocatalysis, with the carbons incorporated into LHCs. After removing lignin and depolymerizing cellulose and hemicelluloses into sugars by acid-hydrolysis, native biomass, including poplar and wheat straw, is converted to LHCs (Figures 3F and S21). The selectivities of LHCs among the C_1 products are 74% and 65%, respectively. Although most of the sugars from acid-hydrolysis are decomposed to LHCs, some unreacted glucose remained perhaps due to partial poisoning of the Ta-CeO_2 photocatalyst. However, if more robust photocatalysts are developed, this oxidative strategy will enable the splitting of carbohydrate C–C bonds more successfully.

Photoreforming of LHCs to H_2 and CO_2

The obtained aqueous solution of LHCs is convenient for transportation to where H_2 is necessary. Decomposition of LHCs to H_2 also circumvents tedious and energy-intensive separation of the products from water. The aqueous solution of LHCs obtained from photocatalytic glucose oxidation was directly used for photocatalytic H_2 generation after filtrating the Ta-CeO_2 photocatalyst. When using Pt/P25 as the photocatalyst or Ru-complex as the thermocatalyst to catalyze H_2 generation, LHCs are almost quantitatively decomposed with H_2 release; relative to the theoretical value of hypothetical photoreforming of glucose ($C_6H_{12}O_6 + 6\,H_2O \rightarrow 12\,H_2 + 6\,CO_2$), the H_2 yields are 33% and 30%, respectively. Along with H_2 production, almost all the carbons in LHCs are converted to CO_2 (Figure 4A). Direct H_2 production from glucose was used as a comparison to highlight the advantages of the stepwise method (Figure 4B). The Pt/P25 was used as the photocatalyst since it has been widely reported for photocatalytic H_2 production from carbohydrates.[18] The amount of H_2 from the direct photoreforming of glucose (13% yield of H_2 after 12 h) is about 0.39-fold of that obtained by the stepwise method, even the first oxidation step consumes part of hydrogen atoms and reduces the theoretical yield of H_2. This result illustrates the significance of breaking C–C bond first in the stepwise photocatalytic H_2 production from biomass.

Solar-light-driven glucose oxidation to C_1 LHCs

The large-scale genuine solar-driven reactions require well-designed reactors.[39,40] We established a lab-scale flow-type apparatus to prove the feasibility of exploiting solar energy for LHCs production from glucose. A Fresnel lens with a size of 1,100 mm × 1,100 mm was used to concentrate solar light and provide sufficient temperature for photocatalytic glucose oxidation. The flow reactor is a quartz coil tube and is installed in an insulating vessel coated with light-absorbing materials to convert the residual solar light into heat. During experiments, the window of the vessel overlaps with the focal point of the Fresnel lens, thereby ensuring maximum utilization of solar energy (Figure 4C). The temperature at the outlet of the reaction tube and the intensity of solar light were recorded to monitor the fluctuant intensity of solar light during solar-light-driven glucose oxidation

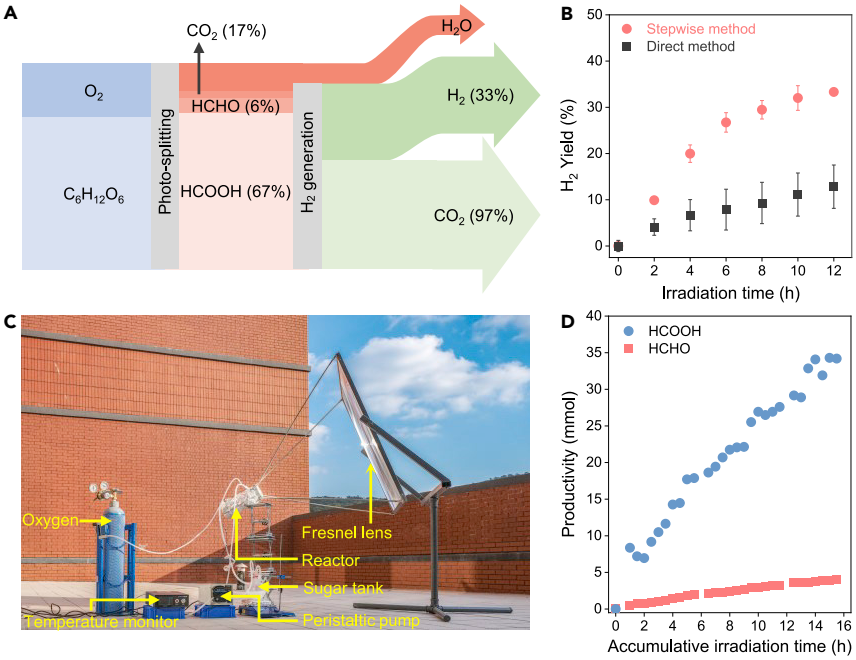

Figure 4. Photocatalytic glucose decomposition to H_2 and CO_2 and solar-light-driven glucose oxidation to C_1 LHCs

(A) Mass flow of the photocatalytic glucose decomposition to H_2 and CO_2. The values in parentheses represent the yields of products. The yield of H_2 is relative to the theoretical value of hypothetical photoreforming of glucose ($C_6H_{12}O_6 + 6H_2O \rightarrow 12H_2 + 6CO_2$).

(B) Stepwise photoassisted decomposition of glucose to H_2 versus direct photoreforming of glucose. Reaction conditions: 1.5 mmol of glucose or LHCs from photocatalytic glucose oxidation, 250 mg of Pt/P25, 25 mL of H_2O, LEDs (365 $\pm$ 10 nm, 40 mW cm^{-2}), and Ar.

(C) Photograph of the flow reaction apparatus equipped with a unit focusing solar light.

(D) Reaction results of flow-type glucose oxidation driven by concentrated solar light. Reaction conditions: 56 mmol L^{-1} of glucose, 8.0 g L^{-1} of Ta-CeO_2, and the flow rates of glucose solution and oxygen were 25 and 5 mL min^{-1}, respectively. The reaction ran for a total of 15.5 h over 3 days. The measured average intensity of solar light was 46 mW cm^{-2}, corresponding to 8.6 kWh of solar light irradiated to the reactor during photocatalytic glucose oxidation.

(Figure S23A). At the beginning of the experiment, the temperature at the outlet of the reaction tube increased to 87°C after continuous irradiation for 1 h, then fluctuated around 100°C due to occasional partial clouds that influence the balance between solar light irradiation and heat dissipation (Figure S23C). Under solar irradiation, glucose was converted to HCOOH and HCHO with formation rates of 2.2 and 0.3 mmol h^{-1}, respectively. The selectivity of LHCs remains at 78% (70% HCOOH selectivity and 8% HCHO selectivity), similar to the results of batch reaction. After 3-day solar light irradiation for a cumulative irradiation time of 15.5 h, the yield of LHCs reached 15%, with 19% of glucose being converted (Figure 4D). The solar-light-driven glucose oxidation to LHCs demonstrates the feasibility of solely utilizing solar energy to provide the thermal and photoenergy to power a heat-promoted photoreaction.

Life cycle assessment of GHG emission

The life cycle greenhouse gas (GHG) emissions in the stepwise photoassisted decomposition of carbohydrates to H_2 were estimated, with detailed information shown in Figure S24 and Table S6. The photocatalytic H_2 production process was integrated with three kinds of biomass pretreating technologies and two kinds of technologies for CO_2 and H_2 separation, generating 6 scenarios for H_2 generation from

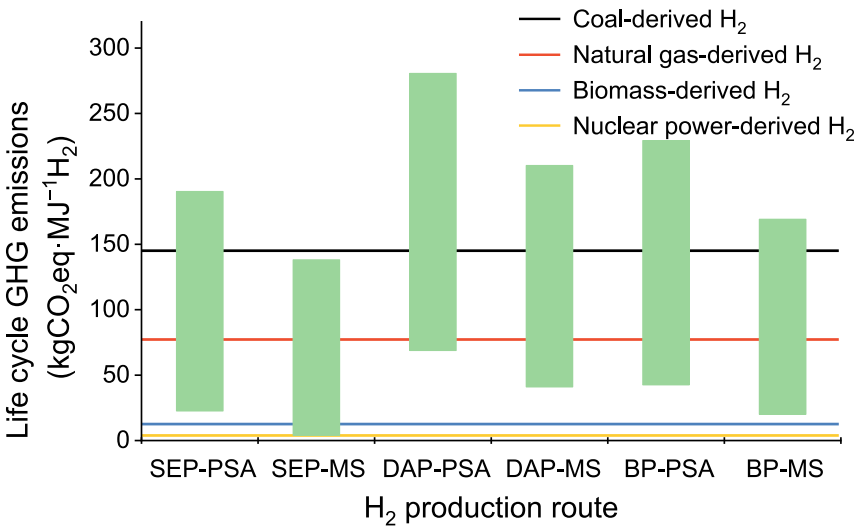

Figure 5. LCA of the GHG emissions of the stepwise photoassisted decomposition of carbohydrates to H_2

SEP-PSA, steam explosion combines with pressure swing adsorption; SEP-MS, steam explosion combines with membrane separation; DAP-PSA, dilute acid pretreatment combines with pressure swing adsorption; DAP-MS, dilute acid pretreatment combines with membrane separation; BP-PSA, biological pretreatment combines with pressure swing adsorption; BP-MS, biological pretreatment combines with membrane separation.

stover (Table S6). The corresponding life cycle GHG emissions were shown in Figure 5. The proposed photocatalytic routes for H_2 production from stover release 4–280 $kgCO_2eq$ per MJ of H_2 in their life cycle models, which cover the life cycle GHG emissions of conventional H_2 production routes, such as coal-derived and natural gas-derived H_2. In the scenario steam explosion combines with membrane separation (SEP-MS), the proposed photocatalytic route emits less GHGs than the mature coal-derived H_2 route, although we adopted a low yield of C_1 LHCs (33%). Compared with potential routes, such as H_2 production via biomass gasification or powered by nuclear energy, the proposed photocatalytic route shows poor mitigation potential of GHG emissions. However, when H_2 yield approximates the theoretical value (65%), the proposed photocatalytic route emits the least life cycle GHGs in scenario SEP-MS. The result implies that future work should focus on more advanced photocatalysts that tolerate the impurities in the sugar mixture from biomass pretreatment, thereby delivering a high H_2 yield from carbohydrates.

To elucidate the GHG emission mitigation potential, the individual contribution of each stage in the life cycle GHG emissions of the proposed photocatalytic route was revealed to determine the main carbon emission processes (Figure S25). Stover pretreatment accounts for the primary contribution (64.1%–81.4%) to the life cycle GHG emissions of the proposed photocatalytic route, illustrating advanced methods for biomass pretreatment are significant for biomass utilization. Among the three pretreating methods, SEP is the most efficient method that integrates with the proposed photocatalytic route. Apart from stover pretreatment, stover acquisition and sugar conversion to C_1 LHCs are responsible for 10%–15% and 6%–14% of the life cycle GHG emissions, respectively. This result highlights the significance of improving the overall H_2 yield from carbohydrates since when more H_2 is obtained from biomass, less energy is consumed for biomass acquisition and pretreatment. Therefore, apart from improving the H_2 generation rate, focusing on

improving H_2 yield is also significant from the perspective of life cycle GHG emissions of H_2 production from biomass. The hydrogen production and separation processes contribute a minor share, especially in the scenario with membrane separation. Overall, the proposed photocatalytic route shows mitigation potential of GHG emissions and practical challenges. Future work should focus on avoiding biomass pretreatment technologies and developing more advanced photocatalysts that tolerate poisons in sugar mixtures.

Conclusions

In this study, we demonstrated the significance of prioritized scission of C–C bonds in carbohydrates for photocatalytic hydrogen production and storage. This C–C bond first strategy emphasizes prioritized biomass conversion to liquid C_1 LHCs via fully breaking the C–C bonds. A synergistic Ta-CeO_2 that utilizes the photoenergy and thermal energy from solar light fully breaks the C–C bonds of carbohydrates, producing C_1 LHCs comprising HCOOH and HCHO in yields from 62% to 86%. During photocatalytic oxidation of carbohydrates, the elevated temperature was adopted to inhibit deleterious radical coupling over the strongly distorted Ta-CeO_2. The resulting C_1 LHCs that can be transported release only H_2 and CO_2, independent of solar light irradiation. The yield of H_2 from glucose is 33%, much higher than that of direct photoreforming of glucose. This stepwise method was also exemplified by flow-type photocatalytic oxidation of glucose under concentrated solar light, which enabled 15% yield of C_1 LHCs from glucose via a cumulative irradiation time of 15.5 h. This work opens the door to hydrogen production and storage by emphasizing the significance of the prioritized scission of biomass C–C bonds.

EXPERIMENTAL PROCEDURES

Resource availability

Lead contact

Further information and requests for resources and materials should be directed to and will be fulfilled by the lead contact, Feng Wang (wangfeng@dicp.ac.cn).

Materials availability

This study did not generate new unique reagents.

Data and code availability

The data generated during this study are available in the main text and the supplemental information.

Preparation of Ta-CeO_2

The Ta-CeO_2 was synthesized by a hydrothermal method. Briefly, $Ce(NO_3)_3 \cdot 6H_2O$ (4.30 g) and $TaCl_5$ (35.8 mg) were dissolved in 100 mL of ethanol. The precursor solution was then mixed with $NH_3 \cdot H_2O$ solution (7.4 mmol L^{-1}) by advection pump followed by centrifugation to obtain a purple slurry. Thereafter, the centrifuged gel was dispersed in 80 mL of ethylene glycol, before being transferred into a 120-mL stainless Teflon-lined autoclave, which was tightly sealed, and heated at 150°C for 48 h. After the reaction, the autoclave was naturally cooled to room temperature, the solid was washed with deionized water until the pH became neutral. A yellow solid powder was obtained after being dried overnight at 100°C and calcined in muffle at 400°C for 2 h with a ramp rate of 10°C min^{-1}.

Photocatalytic oxidation of bio-polyols and sugars to C_1 LHCs

Photocatalytic oxidation of bio-polyols and sugars was conducted in homemade photoreactors (Figure S6A) with top photoirradiation (blue LEDs with a wavelength

of 452 ± 10 nm, the radial distribution of light intensity was shown in Figure S6B; the indicated light intensity represents that of the center point). Bottom heating was used to keep the system at desired temperature. For a typical reaction, 50 mg of catalyst, substrate (bio-polyols or sugars containing 9 mmol of carbons), 25 mL of deionized water, and a stir bar were added into a 100-mL Teflon-lined stainless autoclave. After being tightly sealed, the atmosphere of the autoclave was replaced with O_2. Thereafter, CH_4, proved to be unreactive and unable to be generated in the reaction system, was used as the internal standard for gas quantification. 5 mL of CH_4 was injected into the reactor by a gas-tight syringe before inflating the reactor with 5 bar of O_2. Preliminary experiments confirmed the absence of CH_4 in the reaction products. CH_4 was also proved to be stable by blank experiments using the same volume fraction of methane and Ta-CeO_2 under the reaction conditions identical to those of photocatalytic oxidation of bio-polyols and sugars. The reactor was preheated to the desired temperature before being irradiated by LEDs under stirring (400 r min^{-1}). After reaction, the autoclave was cooled to room temperature naturally.

Hydrogen generation from solution after photocatalytic glucose oxidation

The C_1 solution from the photocatalytic oxidation of glucose is directly used for catalytic hydrogen generation after removing the photocatalyst by centrifugation.

Photocatalytic LHCs decomposition to H_2. Typically, 25 mL of the LHCs solution and 250 mg of Pt/P25 were added into a 220 mL-quartz cell. After being tightly sealed, the atmosphere of the quartz cell was replaced by Ar. The internal standards, including 50 mL of He and 5 mL of CH_4, were injected into the quartz cell by a gas-tight syringe. The quartz cell was then top-irradiated by 365 nm LEDs (40 mW cm^{-2}) under stirring (400 r min^{-1}). The reaction temperature was kept at room temperature by circulating condensed water. After reaction, 50 μL of gas sample was analyzed by GC every 2 h for the quantification of H_2; CO_2 was quantified after reaction. Direct photocatalytic H_2 production from decomposing glucose was used as a comparison. In this experiment, glucose solution (25 mL, 0.06 mmol mL^{-1}) was used instead.

Thermocatalytic LHCs decomposition to H_2. Typically, 25 mL of LHCs and 50 μmol of the Ru-complex were added into a 100-mL Teflon-lined stainless autoclave. After being tightly sealed, the reaction system was replaced by Ar. 50 mL of He as internal standard was injected into the reactor by a gas-tight syringe. Then the reactor was heated at 95°C under stirring (400 r min^{-1}); H_2 was quantified after 10 h of reaction.

Measurement of E_a of photocatalytic glycerol oxidation

The rate constants were measured at different reaction temperatures under the irradiation of blue LEDs with light intensities of 10 and 200 mW cm^{-2}, respectively. Briefly, 3 mmol of glycerol and 50 mg of Ta-CeO_2 were added into a Teflon-lined autoclave containing 25 mL of deionized water. After replacing the atmosphere with 5 bar of O_2, the autoclave was preheated to desired temperature and then top-irradiated with blue LEDs (452 ± 10 nm). After reaction, glycerol was quantified by the methods described above.

To calculate the apparent activation energy for glycerol conversion, the logarithm of the glycerol concentration ($\ln C_{glycerol}$) was plotted against the reaction time. The found linear relationship (Figure S19) conforms to first-order reaction kinetics; the slope of the line is the corresponding reaction rate constant (k). The E_a of photo glycerol oxidation was obtained using the Arrhenius equation.

The first-order reaction rate formula and the Arrhenius equation are shown below:

$$\ln C_{glycerol} = -kt + b \quad \text{(Equation 1)}$$

$$\ln k = -\frac{E_a}{RT} + C \quad \text{(Equation 2)}$$

where $C_{glycerol}$ is the glycerol concentration (mol L^{-1}), t is the reaction time (s), k is the reaction rate constant, E_a is the apparent activation energy (kJ mol^{-1}), T is the reaction temperature (K), R is the molar gas constant (J mol^{-1} K^{-1}), b and C are constants.

Glucose flow reaction under concentrated natural solar energy

A solar-light-driven apparatus for flow-type photocatalytic oxidation of glucose was conducted during spring in Dalian, China (N 121.27°, E 38.82°; 10:30–16:00 on 18th, 11:00–16:00 on 19th, and 10:30–13:30 on 20th April 2022). The flow-type apparatus contains a Fresnel lens, a quartz coil tube, a sugar tank, a peristaltic pump, a temperature monitor and an oxygen tank. The quartz coil tube is installed in an insulating vessel coated with light-absorbing materials; the window area of the vessel is 2,500 mm^2. Solar light was concentrated to a spot with a diameter of 10 mm by a Fresnel lens with a size of 1,100 mm × 1,100 mm. The vessel window overlaps with the light spot to allow maximum utilization of solar light.

To increase the dispersibility of the catalyst and to avoid its precipitation in the reactor, Ta-CeO_2 (6.4 g) was ball-milled for 0.5 h before being suspended in glucose solution (800 mL, 56 mmol L^{-1}). The slurry was cyclically pumped into the coil tube under stirring through a peristaltic pump with a rate of 25 mL min^{-1} (Figure S23A), the volume of every single cycle is 200 mL. Before pumping into the coil tube, the liquid was mixed with O_2 which was input with a rate of 5 mL min^{-1}. At the outlet of the tube, the real-time temperature was detected and the sample was collected. Samples of the reaction solution (2 mL) were collected every 0.5 h; the light intensity and the temperature were recorded at the same time (Figure S23C). HCOOH and HCHO in the samples were analyzed by high-performance liquid chromatography (HPLC) after adding 2 mg of propanol and 2.5 mg of 4-chloroanisole as the internal standards.

Quantitative analysis of products

After reactions, the gas products were collected in a gas bag and analyzed by GC. The liquid phase was diluted with 25 mL of MeCN, followed by the addition of the internal standards. Afterward, the catalyst was filtered out, the supernatant was analyzed by GC and HPLC.

CO_2 and H_2 in the gas phase were quantified with CH_4 and He as internal standards, respectively. The two products were analyzed by GC (Techcomp 7900, TDX-01 column) equipped with a thermal conductivity detector (TCD). The carrier gas for the quantification of CO_2 and H_2 was He and Ar, respectively.

The produced gas was calculated by the following equation:

$$n = \frac{R_f \times A \times V_i/mL}{A_i} \times \frac{101.3}{8.314 \times 298} mmol \quad \text{(Equation 3)}$$

where n is the amount of gas (in mmol) produced in the reaction system; R_f is the responsive factor of H_2; A and A_i are the TCD responses of produced gas and internal standard, respectively; V_i is the volume of internal standard gas injected into the reactor.

Glycerol was analyzed by GC (Techcomp 7900, PEG-20 M column) equipped with a flame ionization detector (FID). Diethylene glycol was used as internal standard.

Bio-polyols and HCOOH were quantified with propanol as the internal standard and analyzed by HPLC (Agilent 1260 Infinity, equipped with Hi-Plex H column (300 mm × 7.7 mm) and RID-6A refractive index detector) with diluted 0.5 mM H_2SO_4 solution as the mobile phase. A UV detector recorded at 210 nm was used to analyze HCOOH, considering glycerol and HCOOH have the same retention time using the Hi-Plex H column. When glycerol is the substrate, malonic acid and diethylene glycol were used as internal standards to quantify HCOOH and glycerol, respectively. The bio-polyols and HCOOH can be calculated by the following equation:

$$n = \frac{R_f \times A \times m_i}{A_i \times MW} \text{mmol} \quad \text{(Equation 4)}$$

where n is the amount of residual bio-polyols or produced HCOOH in the reaction system (mmol); R_f is the responsive factor of bio-polyols or HCOOH; A and A_i are the FID responses of the bio-polyols/HCOOH and internal standard, respectively; m_i is the mass of internal standard; MW is the relative molecular weight.

HCHO was quantified by a derivatization method with 4-chloroanisole as the internal standard. Typically, 50 μL of the reaction liquid was mixed with 1 mL of MeCN solution containing 2,4-dinitrophenylhydrazine (2,4-DNPH, 5 μmol mL^{-1}) and acetic acid (1.3 mmol mL^{-1}). The mixture was then heated in a water bath (50°C) for 60 min to completely convert HCHO and 2,4-DNPH into formaldehyde-2,4-dinitrophenyhydrazone (F-DNPH) which is stable for analysis.

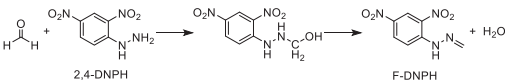

After the derivatization reaction, the mixture was filtered with a 0.22 μm Nylon syringe filter; the filtrate was analyzed by HPLC (Agilent 1260 Infinity, equipped with XSelect HSS PFP column and a UV detector recorded at 232 nm). The mixture consisting of acetonitrile and water (45:55 v/v) is the mobile phase. The produced HCHO can be calculated by the following equation:

$$n_{HCHO} = \frac{R_f \times A_{HCHO} \times m_{4-chloroanisole}}{A_{4-chloroanisole} \times MW} \text{mmol} \quad \text{(Equation 5)}$$

where n_{HCHO} represents the amount of F-DNPH, of which the amount is equal to HCHO produced in the photocatalytic reactions; R_f is the responsive factor of F-DNPH; A_{HCHO} and $A_{4\text{-chloroanisole}}$ are the UV responses of F-DNPH and 4-chloroanisole, respectively; $m_{4\text{-chloroanisole}}$ is the mass of 4-chloroanisole added to the reaction, and MW is the relative molecular mass of F-DNPH.

Calculation of conversion and yield

The conversion of bio-polyols, the yield of products, the selectivity of LHCs, and the carbon balance of the reaction are calculated as follows:

$$\text{Conversion} = \left(1 - \frac{n}{n_0}\right) \times 100\% \quad \text{(Equation 6)}$$

$$\text{Yield} = \frac{n_{Product}}{n_0 \times a} \times 100\% \quad \text{(Equation 7)}$$

$$\text{Selectivity of LHCs} = \frac{\text{Yield of HCOOH} + \text{Yield of HCHO}}{\text{Conversion}} \times 100\% \quad \text{(Equation 8)}$$

$$\text{Carbon balance} = \frac{\text{Yield of HCOOH} + \text{Yield of HCHO} + \text{Yield of } CO_2}{\text{Conversion}} \times 100\% \quad \text{(Equation 9)}$$

where n_0 and n represent the moles of feedstock before and after the reaction (in mmol), respectively; $n_{Product}$ is the amount of product produced after reaction, and a represents the ratio of the carbon atoms in the substrate and the product.

HAADF-STEM

Samples for TEM were prepared by dispersing catalyst in ethanol and sonication for 10 min. The suspension (15 μL) was loaded onto a Cu TEM grid and dried. HAADF-STEM images were obtained using a JEM-F200 operated at 200 kV.

XAS

Samples for X-ray absorption spectroscopy (XAS) experiments at the Ta L_3 edge have been performed at SAMBA beamline of Synchrotron SOLEIL.[41] Two Pd mirrors have been set at 4 mrad to reject harmonics, the monochromator was equipped with Si (220) crystals, and measurements have been performed in fluorescence mode with a 35 pixels HPGe detector (Mirion/Canberra) in conjunction with DxMap DSP (XIA), while ionization chambers were filled with nitrogen at 1 bar (7.5% absorption at 12 keV). Measurements of reference materials have been performed in transmission mode. In order to refine EXAFS, the XAFS spectrum of Ta-CeO_2 has been analyzed using the DEMETER suite (Athena to extract signal, Artemis to refine the fit). The S_0^2 has been deduced from a fitting on a tantalum foil.

SUPPLEMENTAL INFORMATION

Supplemental information can be found online at https://doi.org/10.1016/j.joule.2023.01.002.

ACKNOWLEDGMENTS

We acknowledge the financial support from the Ministry of Science and Technology of the People's Republic of China (2018YFE0118100), the National Natural Science Foundation of China (22025206, 21721004, 21991094, 21991090, 22172157, and 22002159), the Joint Fund of the Yulin University and the Dalian National Laboratory for Clean Energy (Grant YLU-DNL Fund 2021019), the Foreign Expert Project (G2022008003), the Fundamental Research Funds for the Central Universities (20720220008), the K.C. Wong Education Foundation of Chinese Academy of Sciences (GJTD-2020-08), and the Italian Ministry of Foreign Affairs and International Cooperation-Project Italy-China n° (CN19GR04). We also thank the instrumental support of the Liaoning Key Laboratory of Biomass Conversion for Energy and Material and the provision of beamtime by Synchrotron SOLEIL.

AUTHOR CONTRIBUTIONS

F.W. and N.L. conceived the idea and designed the experiments. P.R. performed the experiments of the main catalytic research and wrote the manuscript under the guidance of N.L. P.R. and Z.G. performed the flow reaction. T.M. and E.F. conducted and analyzed the EXAFS data. Z.Z. performed the LCA. N.T. characterized the catalyst with HAADF-STEM. Y.H. performed the DFT calculations. P.F. participated in the discussion of the experimental details and the framework of the work. All the authors

contributed to the discussion of the experimental work and the final write-up of the manuscript.

DECLARATION OF INTERESTS

The authors declare no competing interests.

INCLUSION AND DIVERSITY

We support inclusive, diverse, and equitable conduct of research.

Received: October 27, 2022
Revised: December 13, 2022
Accepted: January 6, 2023
Published: January 31, 2023

REFERENCES

1. Turner, J.A. (2004). Sustainable hydrogen production. Science *305*, 972–974. https://doi.org/10.1126/science.1103197.

2. Liu, W., Cui, Y., Du, X., Zhang, Z., Chao, Z.S., and Deng, Y.L. (2016). High efficiency hydrogen evolution from native biomass electrolysis. Energy Environ. Sci. *9*, 467–472. https://doi.org/10.1039/C5EE03019F.

3. Chen, Z., Li, P., Anderson, R., Wang, X., Zhang, X., Robison, L., Redfern, L.R., Moribe, S., Islamoglu, T., Gómez-Gualdrón, D.A., et al. (2020). Balancing volumetric and gravimetric uptake in highly porous materials for clean energy. Science *368*, 297–303. https://doi.org/10.1126/science.aaz8881.

4. Fein, D.E., and Wachs, I.E. (2002). Quantitative determination of the catalytic activity of bulk metal oxides for formic acid oxidation. J. Catal. *210*, 241–254. https://doi.org/10.1006/jcat.2002.3683.

5. Zhou, J., and Mullins, D.R. (2006). Adsorption and reaction of formaldehyde on thin-film cerium oxide. Surf. Sci. *600*, 1540–1546. https://doi.org/10.1016/j.susc.2006.02.009.

6. Kumar, A., Daw, P., and Milstein, D. (2022). Homogeneous catalysis for sustainable energy: hydrogen and methanol economies, fuels from biomass, and related topics. Chem. Rev. *122*, 385–441. https://doi.org/10.1021/acs.chemrev.1c00412.

7. Boddien, A., Mellmann, D., Gärtner, F., Jackstell, R., Junge, H., Dyson, P.J., Laurenczy, G., Ludwig, R., and Beller, M. (2011). Efficient dehydrogenation of formic acid using an iron catalyst. Science *333*, 1733–1736. https://doi.org/10.1126/science.1206613.

8. Wei, D., Sang, R., Sponholz, P., Junge, H., and Beller, M. (2022). Reversible hydrogenation of carbon dioxide to formic acid using a Mn-pincer complex in the presence of lysine. Nat. Energy *7*, 438–447. https://doi.org/10.1038/s41560-022-01019-4.

9. Zhang, P., Guo, Y.-J., Chen, J., Zhao, Y.-R., Chang, J., Junge, H., Beller, M., and Li, Y. (2018). Streamlined hydrogen production from biomass. Nat. Catal. *1*, 332–338. https://doi.org/10.1038/s41929-018-0062-0.

10. Han, X., Sheng, H., Yu, C., Walker, T.W., Huber, G.W., Qiu, J., and Jin, S. (2020). Electrocatalytic oxidation of glycerol to formic acid by $CuCo_2O_4$ spinel oxide nanostructure catalysts. ACS Catal. *10*, 6741–6752. https://doi.org/10.1021/acscatal.0c01498.

11. Huber, G.W., Shabaker, J.W., and Dumesic, J.A. (2003). Raney Ni-Sn catalyst for H_2 production from biomass-derived hydrocarbons. Science *300*, 2075–2077. https://doi.org/10.1126/science.1085597.

12. Liao, Y., Koelewijn, S.F., Van den Bossche, G., Van Aelst, J., Van den Bosch, S., Renders, T., Navare, K., Nicolaï, T., Van Aelst, K., Maesen, M., et al. (2020). A sustainable wood biorefinery for low-carbon footprint chemicals production. Science *367*, 1385–1390. https://doi.org/10.1126/science.aau1567.

13. Zhang, Z., and Huber, G.W. (2018). Catalytic oxidation of carbohydrates into organic acids and furan chemicals. Chem. Soc. Rev. *47*, 1351–1390. https://doi.org/10.1039/C7CS00213K.

14. Hou, Y., Niu, M., and Wu, W. (2020). Catalytic oxidation of biomass to formic acid using O_2 as an oxidant. Ind. Eng. Chem. Res. *59*, 16899–16910. https://doi.org/10.1021/acs.iecr.0c01088.

15. Nosaka, Y., and Nosaka, A.Y. (2017). Generation and detection of reactive oxygen species in photocatalysis. Chem. Rev. *117*, 11302–11336. https://doi.org/10.1021/acs.chemrev.7b00161.

16. Uekert, T., Pichler, C.M., Schubert, T., and Reisner, E. (2020). Solar-driven reforming of solid waste for a sustainable future. Nat. Sustain. *4*, 383–391. https://doi.org/10.1038/s41893-020-00650-x.

17. Wakerley, D.W., Kuehnel, M.F., Orchard, K.L., Ly, K.H., Rosser, T.E., and Reisner, E. (2017). Solar-driven reforming of lignocellulose to H_2 with a CdS/CdO_x photocatalyst. Nat. Energy *2*, 17021. https://doi.org/10.1038/nenergy.2017.21.

18. Kuehnel, M.F., and Reisner, E. (2018). Solar hydrogen generation from lignocellulose. Angew. Chem. Int. Ed. Engl. *57*, 3290–3296. https://doi.org/10.1002/anie.201710133.

19. Zhang, K., Chang, L., An, Q., Wang, X., and Zuo, Z. (2019). Dehydroxymethylation of alcohols enabled by cerium photocatalysis. J. Am. Chem. Soc. *141*, 10556–10564. https://doi.org/10.1021/jacs.9b05932.

20. Nguyen, S.T., Murray, P.R.D., and Knowles, R.R. (2020). Light-driven depolymerization of native lignin enabled by proton-coupled electron transfer. ACS Catal. *10*, 800–805. https://doi.org/10.1021/acscatal.9b04813.

21. Kisch, H. (2017). Semiconductor photocatalysis for chemoselective radical coupling reactions. Acc. Chem. Res. *50*, 1002–1010. https://doi.org/10.1021/acs.accounts.7b00023.

22. Luo, N., Nie, W., Mu, J., Liu, S., Li, M., Zhang, J., Gao, Z., Fan, F., and Wang, F. (2022). Low-work function metals boost selective and fast scission of methanol C–H bonds. ACS Catal. *12*, 6375–6384. https://doi.org/10.1021/acscatal.1c06005.

23. Huang, Z., Luo, N., Zhang, C., and Wang, F. (2022). Radical generation and fate control for photocatalytic biomass conversion. Nat. Rev. Chem. *6*, 197–214. https://doi.org/10.1038/s41570-022-00359-9.

24. Cao, S., Chen, Y., Wang, H., Chen, J., Shi, X., Li, H., Cheng, P., Liu, X., Liu, M., and Piao, L. (2018). Ultrasmall CoP nanoparticles as efficient cocatalysts for photocatalytic formic acid dehydrogenation. Joule *2*, 549–557. https://doi.org/10.1016/j.joule.2018.01.007.

25. Kar, S., Rauch, M., Leitus, G., Ben-David, Y., and Milstein, D. (2021). Highly efficient additive-free dehydrogenation of neat formic acid. Nat. Catal. *4*, 193–201. https://doi.org/10.1038/s41929-021-00575-4.

26. Wang, M., Liu, M., Lu, J., and Wang, F. (2020). Photo splitting of bio-polyols and sugars to methanol and syngas. Nat. Commun. *11*, 1083. https://doi.org/10.1038/s41467-020-14915-8.

27. Shahin, A.M., Grandjean, F., Long, G.J., and Schuman, T.P. (2005). Cerium L_{III}-edge XAS investigation of the structure of crystalline and amorphous cerium oxides. Chem. Mater. *17*, 315–321. https://doi.org/10.1021/cm0492437.

28. Shannon, R.D. (1976). Revised effective ionic radii and systematic studies of interatomic distances in halides and chalcogenides. Acta

Cryst. A *32*, 751–767. https://doi.org/10.1107/S0567739476001551.

29. Montini, T., Gombac, V., Sordelli, L., Delgado, J.J., Chen, X., Adami, G., and Fornasiero, P. (2011). Nanostructured Cu/TiO_2 photocatalysts for H_2 production from ethanol and glycerol aqueous solutions. ChemCatChem *3*, 574–577. https://doi.org/10.1002/cctc.201000289.

30. Campbell, C.T., and Peden, C.H. (2005). Chemistry. Oxygen vacancies and catalysis on ceria surfaces. Science *309*, 713–714. https://doi.org/10.1126/science.1113955.

31. Yang, C., Yu, X., Pleßow, P.N., Heißler, S., Weidler, P.G., Nefedov, A., Studt, F., Wang, Y., and Wöll, C. (2017). Rendering photoreactivity to ceria: the role of defects. Angew. Chem. Int. Ed. Engl. *56*, 14301–14305. https://doi.org/10.1002/anie.201707965.

32. Xie, S., Wang, Z., Cheng, F., Zhang, P., Mai, W., and Tong, Y. (2017). Ceria and ceria-based nanostructured materials for photoenergy applications. Nano Energy *34*, 313–337. https://doi.org/10.1016/j.nanoen.2017.02.029.

33. Bu, Y.B., Chen, Y.F., Jiang, G.M., Hou, X.M., Li, S., and Zhang, Z.T. (2020). Understanding of Au-CeO_2 interface and its role in catalytic oxidation of formaldehyde. Appl. Catal. B *260*, 118138. https://doi.org/10.1016/j.apcatb.2019.118138.

34. Luo, N., Montini, T., Zhang, J., Fornasiero, P., Fonda, E., Hou, T., Nie, W., Lu, J., Liu, J., Heggen, M., et al. (2019). Visible-light-driven coproduction of diesel precursors and hydrogen from lignocellulose-derived methylfurans. Nat. Energy *4*, 575–584. https://doi.org/10.1038/s41560-019-0403-5.

35. Liao, F., Lo, T.W.B., Sexton, D., Qu, J., Wu, C.-T., and Tsang, S.C.E. (2015). PdFe nanoparticles as selective catalysts for C–C cleavage in hydrogenolysis of vicinal diol units in biomass-derived chemicals. Catal. Sci. Technol. *5*, 887–896. https://doi.org/10.1039/C4CY01159G.

36. Li, Z., Yan, Y., Xu, S.M., Zhou, H., Xu, M., Ma, L., Shao, M., Kong, X., Wang, B., Zheng, L., et al. (2022). Alcohols electrooxidation coupled with H_2 production at high current densities promoted by a cooperative catalyst. Nat. Commun. *13*, 147. https://doi.org/10.1038/s41467-021-27806-3.

37. Liu, M., Wang, Y., Kong, X., Rashid, R.T., Chu, S., Li, C.-C., Hearne, Z., Guo, H., Mi, Z., and Li, C.-J. (2019). Direct catalytic methanol-to-ethanol photo-conversion via methyl carbene. Chem *5*, 858–867. https://doi.org/10.1016/j.chempr.2019.01.005.

38. Park, H., Yun, Y.S., Kim, T.Y., Lee, K.R., Baek, J., and Yi, J. (2015). Kinetics of the dehydration of glycerol over acid catalysts with an investigation of deactivation mechanism by coke. Appl. Catal. B *176–177*, 1–10. https://doi.org/10.1016/j.apcatb.2015.03.046.

39. Goto, Y., Hisatomi, T., Wang, Q., Higashi, T., Ishikiriyama, K., Maeda, T., Sakata, Y., Okunaka, S., Tokudome, H., Katayama, M., et al. (2018). A particulate photocatalyst water-splitting panel for large-scale solar hydrogen generation. Joule *2*, 509–520. https://doi.org/10.1016/j.joule.2017.12.009.

40. Nishiyama, H., Yamada, T., Nakabayashi, M., Maehara, Y., Yamaguchi, M., Kuromiya, Y., Nagatsuma, Y., Tokudome, H., Akiyama, S., Watanabe, T., et al. (2021). Photocatalytic solar hydrogen production from water on a 100-m^2 scale. Nature *598*, 304–307. https://doi.org/10.1038/s41586-021-03907-3.

41. Briois, V., Fonda, E., Belin, S., Barthe, L., La Fontaine, C., Langlois, F., Ribbens, M., and Villain, F. (2011). SAMBA: the 4–40 keV X-ray Absorption Spectroscopy Beamline at SOLEIL (EDP Sciences), pp. 41–47. https://doi.org/10.1051/uvx/2011006.